RESEARCH ARTICLE

ADVANCED FUNCTIONAL MATERIALS
www.afm-journal.de

Cephalopod-Inspired Stretchable Self-Morphing Skin Via Embedded Printing and Twisted Spiral Artificial Muscles

Fan Fei, Parth Kotak, Li He, Xiaofeng Li, Cyan Vanderhoef, Caterina Lamuta, and Xuan Song**

Cutaneous muscles drive the texture-modulation behavior of cephalopods by protruding several millimeters out of the skin. Inspired by cephalopods, a self-morphing, stretchable smart skin containing embedded-printed electrodes and actuated by Twisted Spiral Artificial Muscles (TSAMs) is proposed. Electrothermally actuated TSAMs are manufactured from inexpensive polymer fibers to mimic the papillae muscles of cephalopods. These spirals can produce strains of nearly 2000% using a voltage of only 0.02 V mm^{-1}. Stretchable and low-resistance liquid metal electrodes are embedded-printed inside the self-morphing skin to facilitate the electrothermal actuation of TSAMs. Theoretical and numerical models are proposed to describe the embedded printing of low-viscosity Newtonian liquid metals as conductive electrodes in a soft elastomeric substrate. Experimental mechanical tests are performed to demonstrate the robustness and electrical stability of the electrodes. Two smart skin prototypes are fabricated to highlight the capabilities of the proposed self-morphing system, including a texture-modulating wearable soft glove and a waterproof skin that emulates the texture-modulation behavior of octopi underwater. The proposed self-morphing stretchable smart skin can find use in a wide range of applications, such as refreshable Braille displays, haptic feedback devices, turbulence tripping, and antifouling devices for underwater vehicles.

1. Introduction

Cephalopods are often known as masters of camouflage due to their ability to control their skin morphology by actuating cutaneous muscles known as papillae, [1] as shown in **Figure 1**a–c. On contraction, these muscles produce a force normal to the skin surface that leads to the generation of complex textures. The texture-modulation behavior of cephalopods allows them to not only camouflage to their surroundings but also to optimize their swimming efficiency by reducing the hydrodynamic drag on the skin surface.[1] Texture-modulation behavior is an attractive feature for a wide range of applications ranging from miniature underwater robots to refreshable Braille displays, and haptic feedback devices.

A few texture- and shape-morphing technologies have recently been proposed based on different materials and actuation mechanisms. Stimulus-responsive materials, such as hydrogels,[2–4] shape memory polymers,[5] and liquid crystal elastomers,[6] have been employed to induce transformations between prescribed shapes through localized pattern control. These techniques provide simple and effective approaches for shape modulation, but also suffer from specific weaknesses, such as slow response rates, low specific power, high stimulus energy, and low precision control of actuation timing and location. Pikul et al.[7] employed pneumatic actuators to produce synthetic camouflaging skins with texture-morphing capabilities, which exhibited fast actuation rates and high energy densities. However, this technology requires heavy, rigid compressors that drastically reduce device portability. Additionally, devices fabricated using the aforementioned actuators all suffer from a common flaw: they can only generate a small number (usually one or two) of predefined target shapes. Hu et al.[8] recently

---

F. Fei, X. Song
Department of Industrial and Systems Engineering
Iowa Technology Institute
The University of Iowa
Iowa City, IA 52242, USA
E-mail: xuan-song@uiowa.edu

P. Kotak, C. Vanderhoef, C. Lamuta
Department of Mechanical Engineering
The University of Iowa
Iowa City, IA 52242, USA
E-mail: caterina-lamuta@uiowa.edu

The ORCID identification number(s) for the author(s) of this article can be found under https://doi.org/10.1002/adfm.202105528.

DOI: 10.1002/adfm.202105528

L. He
Foshan Nanhai Guangdong University of Technology CNC Equipment Cooperative Innovation Institute
Foshan, Guangdong 528225, China

L. He
School of Electromechanical Engineering
Guangdong University of Technology
Guangzhou, Guangdong 510006, China

X. Li
School of Power and Mechanical Engineering
Wuhan University
Wuhan 430072, China

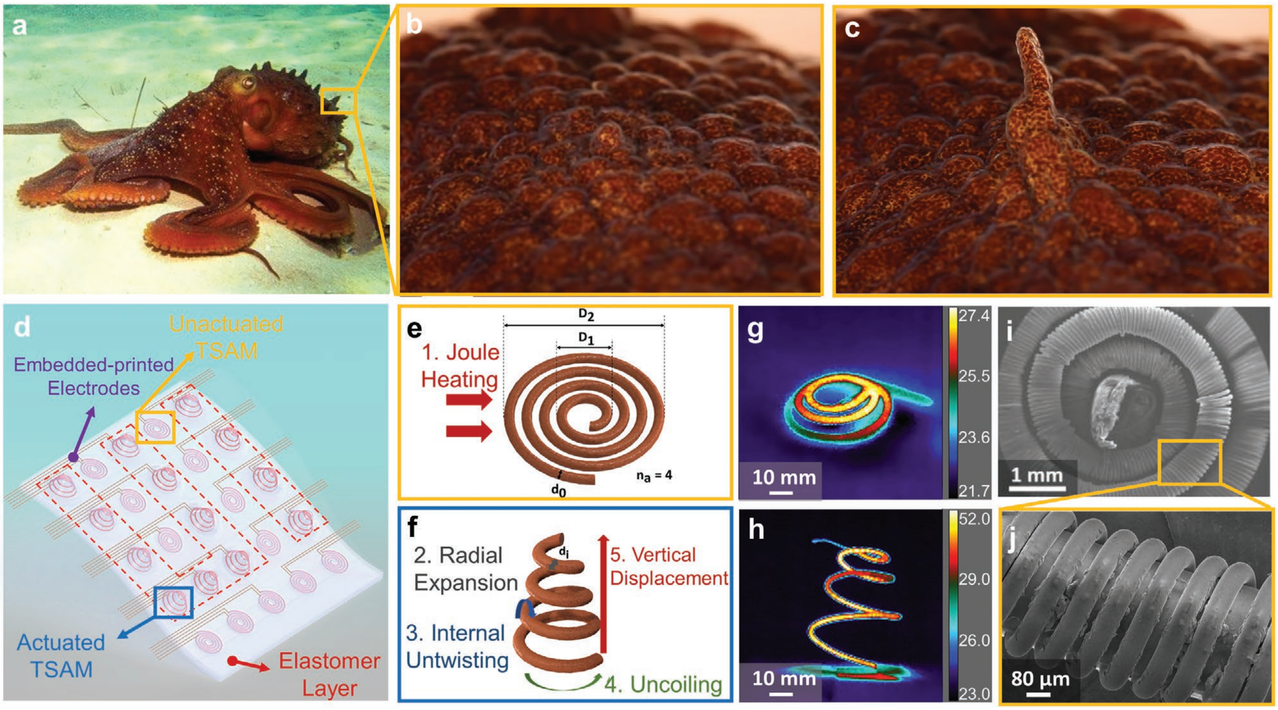

Figure 1. Papillae of cephalopods in nature and TSAMs in cephalopod-inspired stretchable, self-morphing skin. a) Macroctopus maorum, commonly known as the Maori octopus or the New Zealand octopus, with actuated papillae crawling on the ocean floor. Reproduced under terms of the CC-BY license.[24] Copyright 2018, Mark Norman, published by Museums Victoria. Close-up of the b) unactuated and c) actuated cutaneous papillae muscle on the skin of the octopus. Reproduced with permission.[7] Copyright 2017, The Authors, published by AAAS. d) Cephalopod-inspired stretchable, self-morphing smart skin actuated using TSAMs. Schematic description of the working principle of TSAMs from e) a flat Archimedean spiral to f) a telescopic conical spring. On joule heating 1), the TSAM undergoes an anisotropic volume expansion 2). This leads to an internal untwisting 3) that is accompanied by spiral uncoiling 4), which finally causes the vertical displacement 5) of the muscle. Temperature profile of the TSAM g) before and h) after electrothermal actuation. i) SEM image of a TSAM manufactured from nylon monofilament fishing line and helically wrapped with copper for electrical conductivity. j) Zoom-in of the helical wrapping of the copper wire around the nylon fiber.

proposed a soft-skin texture-modulating device actuated by a rotary displacement pump with solenoid valves. Although this solution can provide a high number of output textures, it also requires a heavy, rigid air compressor that significantly limits the mobility of the device.

Inspired by cephalopods, we developed a soft, stretchable, and adaptive self-morphing skin able to overcome the limitations mentioned above in terms of portability, actuation rate, power required, and number of textures/shapes provided. The device is composed of Twisted Spiral Artificial Muscles (TSAMs)[9] and stretchable, highly conductive liquid–metal electrodes and can provide on-demand texture modulation, as illustrated in Figure 1d. TSAMs can produce strains (ratio of the maximum vertical displacement to the initial height, i.e., the fiber diameter, of a TSAM) of nearly 2000% using a voltage of only 0.02 V mm^{-1}. Specifically, TSAMs with a fiber diameter of Φ 0.4 mm used in this work produce a vertical displacement of 10 mm upon electrothermal actuation and depict a strain of 2500%, as shown in Figure S1 (Supporting Information). When assembled to form a matrix of digital texture voxels, TSAMs can provide unlimited textures in the micrometers-to-centimeters range. Electrical actuation of TSAMs is enabled by a liquid–metal electrode network (i.e., eutectic gallium–indium or EGaIn) spatially printed in an elastomeric matrix, which connects the TSAMs to an external power supply. The flexible electrode network features low electrical resistance, and, unlike traditional rigid electrical wire arrays, can undergo large deformation before failure.[10]

A key challenge to fabricating the proposed self-morphing skin lies in printing a complex liquid–metal electrode network in an elastomeric matrix without sacrificing its conductivity. Due to their low-viscosity, Newtonian flow behaviors,[11] liquid metals lack viscosity-recovery capability to retain their shapes after processing shear stress is removed. Numerous efforts have been made to enable the integration of liquid metals with flexible substrates, such as indirect microchannels printing[12–16] and on-surface printing.[17–19] Ota et al.[16] fabricated a flexible substrate with microchannels through conventional 3D printing processes and then filled the microchannels with liquid metals. Tabatabai et al.[17] printed droplets of a liquid alloy on the surface of an elastomer substrate and sealed the liquid with an additional layer of silicone elastomer to prevent it from deforming. These techniques can produce low-resistance electrodes (e.g., 0.07 Ω) in printed materials but involve a multistep fabrication process that limits fabrication efficiency and flexibility. Instead of using pure liquid metals, some researchers adjusted the printability of the materials by adding rheological modifiers and directly printing the resulting materials in an elastomeric reservoir through embedded printing methods.[20–23] The printed electrodes demonstrated large elongation (e.g., ≈700–800%), but also exhibited a high resistivity (e.g., 117 Ω cm) due to the presence of the rheological modifier ingredients, which is too large to electrothermally actuate TSAMs.

In this paper, we propose to utilize an embedded printing process to directly print a low-resistance, stretchable, liquid–metal electrode network in a flexible elastomer. To overcome the aforementioned challenge in printing low-viscosity Newtonian liquid metals, we propose to leverage subregions that enable static crevasse formation in the operation regime of the embedded printing process. EGaIn (Sigma-Aldrich, St. Louis, MO) was used as the ink for printing due to its high conductivity. Commercially available silicone elastomers (i.e., Smooth-On FX-Pro) with predefined amounts of thickening and thinning liquids (refer to Section 4) were chosen as the base and filling elastomers, which are highly deformable, mechanically robust, and chemically and electrically compatible with the EGaIn ink.

2. Results and Discussion

2.1. Device Design: TSAMs and Embedded-Printed Electrodes

A TSAM is comprised of a twisted inexpensive polymer fishing line wrapped with copper wires and is initially flattened into an Archimedean spiral prior to electrical actuation. The actuation mechanism of TSAMs is schematically depicted in Figure 1e,f. Upon heating, the polymer fibers of TSAMs undergo an anisotropic volume expansion, i.e., a large expansion in the radial direction from d_0 (Figure 1e) to d_i (Figure 1f) and a small contraction in the axial direction. The axial contraction of the fibers is much smaller than the radial expansion and can therefore be neglected.[25] Radially expanded TSAMs experience a local untwisting that further leads to spontaneous uncoiling of the fiber. This uncoiling ultimately causes the out-of-plane vertical displacement of the TSAM, as shown in Figure 1f. Figure 1g,h depicts the temperature profile of a 0.8 mm thick TSAM before and after actuation, respectively. Before heating, the TSAM is in the form of a flat spiral, as shown in Figure 1g. Upon electrothermal heating, the TSAM undergoes a volume expansion, leading to a vertical displacement of the TSAM, as shown in Figure 1h. The maximum temperature attained by the TSAM during actuation is 52 °C (this guarantees reversible contraction without causing thermal degradation of the polymer fiber). Figure 1i is a scanning electron microscopy (SEM) image of a TSAM. The helical wrapping of the copper wire around the nylon fiber can be clearly seen in Figure 1j. Additional details on the manufacturing and working mechanism of TSAMs are provided in Section S1 of the Supporting Information.[9,26]

The embedded printing process for fabricating a liquid–metal electrode network is schematically depicted in **Figure 2**a. A printing mold was initially filled with the base elastomer at the bottom and the filling elastomer on the top. During printing (Figure 2a,b), a nozzle was inserted into the base elastomer and traversed along the printing direction at a moving speed v; the EGaIn ink was simultaneously extruded from the nozzle into the base elastomer at a flow rate U. By carefully controlling the printing parameters (e.g., printing speed and flow rate) toward specific subregions in the operation regime, a static, uniform channel can be formed in the base elastomer to hold the extruded ink at a certain depth as the filling elastomer with a low viscosity flows into the channel to seal the printed electrodes (Figure 2b; and Video S1, Supporting Information). To form and seal the channel, the elastomers were adjusted with different yield-stress properties (see detailed data in Section 2.2): the filling elastomer exhibited a liquid-like flow behavior under gravity (Figure 2c), whereas the base elastomer remained thick and static under gravity (Figure 2d). Embedded-printed electrodes in the form of straight lines, a square, a circle, and the letters “UI” are shown in Figure 2e–h, respectively.

2.2. Rheological Behaviors of Base and Filling Elastomers

Figure 3a,b shows that both the base and the filling elastomer exhibited shear-thinning non-Newtonian behaviors. Shear rate $\dot{\gamma}$ during the printing process is dependent on the moving speed of the nozzle v and the diameter d of extruded EGaIn in the elastomer, which is defined by $\dot{\gamma}=\frac{v}{d}$. The moving speed in the printing process was varied between 10 and 60 mm s^{-1}, and the diameter of extruded EGaIn was 0.2 mm. The shear rate in the printing process was determined to be in the range of 50–300 s^{-1}. The corresponding viscosity of the base elastomer was estimated to be between 3 and 25 Pa s, and the viscosity of the filling elastomer was around 7 Pa s.

The amplitude sweep test results shown in Figure 3c suggest that the base elastomer has a yield stress τ_y of 159.25 Pa, which was determined from the crossover point of the storage modulus G′ curve and loss modulus G″ curve.[27,28] When the shear stress applied to the base elastomer was less than the yield stress of 159.25 Pa, its storage modulus G′ was higher than its loss modulus G″, and the base elastomer behaved like a solid elastic material; as the applied shear stress was increased above the yield stress, the loss modulus dominated the storage modulus, indicating a liquid-like behavior of the base elastomer. In comparison, the loss modulus of the filling elastomer was always higher than its storage modulus, indicating a liquid-state behavior of the material. This unique combination of rheological properties of the two elastomers facilitates embedded printing of low-viscosity Newtonian fluids in an elastomer matrix through static crevasse formation in the base elastomer and rapid healing by the filling elastomer.

2.3. Effects of Process Parameters on Printing Morphology

The printing geometries of EGaIn electrodes via embedded printing are strongly impacted by the moving speed v of the nozzle and the flow rate U of the EGaIn material from the nozzle. To understand the effects of these two parameters, different straight EGaIn filaments were printed under varying combinations of v (i.e., 10, 35, and 60 mm s^{-1}) and U (i.e., 3000 and 75 µL min^{-1}), as depicted in Figure 3d,e. When the moving speed was set at 60 mm s^{-1}, all the printed EGaIn filaments were uniform and continuous; increasing the flow rate from 75 to 3000 µL min^{-1} resulted in an increase of the filament diameter from 75 to 200 µm. When the moving speed was small, e.g., 10 or 35 mm s^{-1}, and the flow rate was large, e.g.,

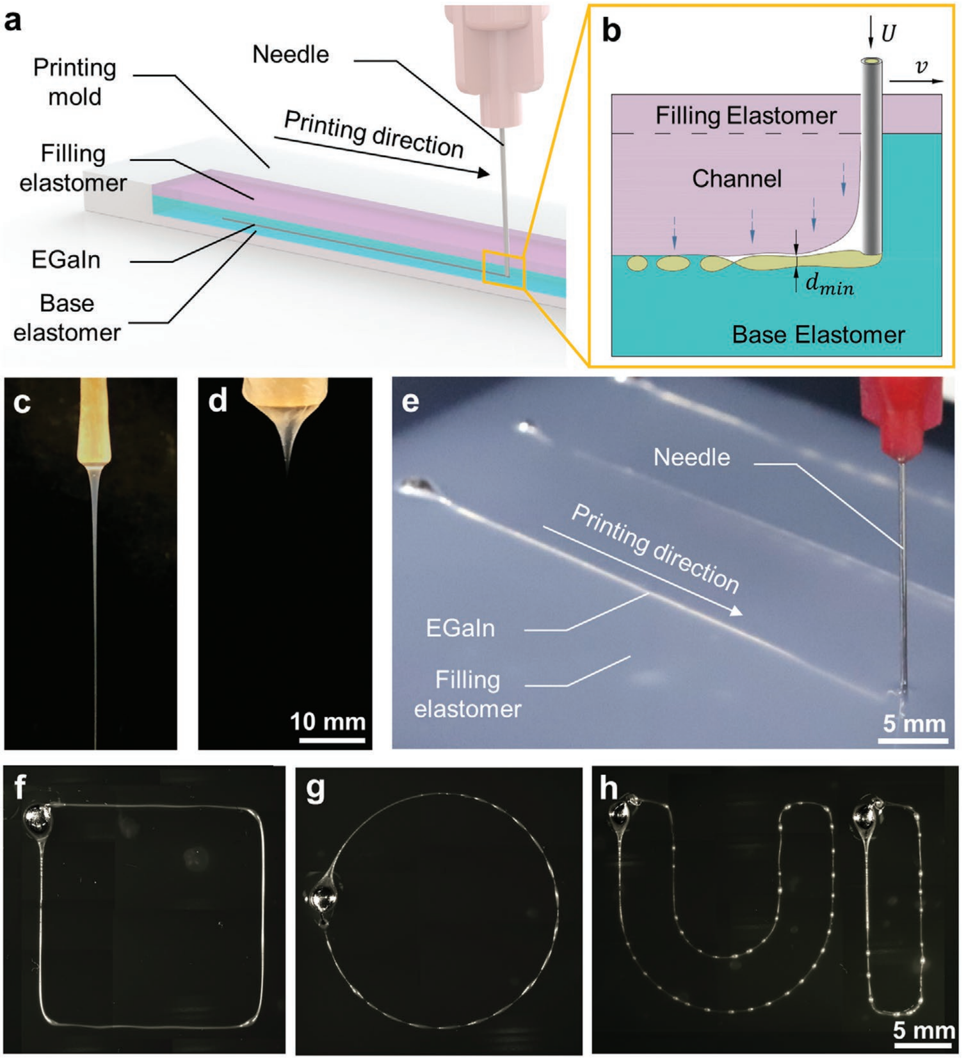

Figure 2. a) Schematic illustration and b) cross-sectional view of the embedded printing process; different rheological behaviors of the c) filling elastomer and d) base elastomer. e) Optical photograph of an array of EGaIn straight-line electrodes fabricated using the proposed process; f) square, g) circle, and h) "UI"-shaped EGaIn printed in the elastomer.

3000 µL min^{-1}, as shown in Figure 3d, extra EGaIn broke the elastomer wall along the crevasse, yielding nonuniform liquid filaments with periodic bulges. A moving speed of 60 mm s^{-1} and a flow rate of 3000 µL min^{-1} were selected to fabricate the test cases in Sections 2.5 and 2.6, which contributed to the highest geometric fidelity.

2.4. Modeling of Embedded Printing for Liquid Metals

2.4.1. Operation Regime of Embedded Printing

To understand the printing morphology of EGaIn and achieve uniform EGaIn electrodes in an elastomer, an operation regime map comprised of extrusion size d and yield stress σ_Y of the base elastomer was defined by four constraint lines (lines 1–4), as shown in Figure 3f. Constraint lines 1 and 2 define the minimum and maximum average diameter of extruded filaments, respectively. When different extrusion sizes were achieved during the embedded printing of liquid metals, an extruded filament underwent two types of failure modes, including filament breakup and filament sinking. Filament breakup results from the effect of surface tension when the extrusion size is small. Constraint line 1 represents the minimum average diameter of extrusion $d_{\min} = \Upsilon/\sigma_Y$ required for the extrusion stability of EGaIn filaments. The region above line 1 (i.e., $d > d_{\min}$) ensures that the beading-up driving force caused by the interfacial tension Υ[29] between extruded EGaIn filaments and the surrounding elastomer is less than the resistance caused by the yield stress σ_Y of surrounding elastomers. This guarantees that the extruded EGaIn filament does not break up into discontinuous droplets along the filament extend axis and maintains a continuous filament shape.[30]

Extruded filaments with an average extrusion size greater than $d_{\min}$ do not fail by breaking up into droplets but can sink to the bottom under gravity (see the inset in Figure 3f; and

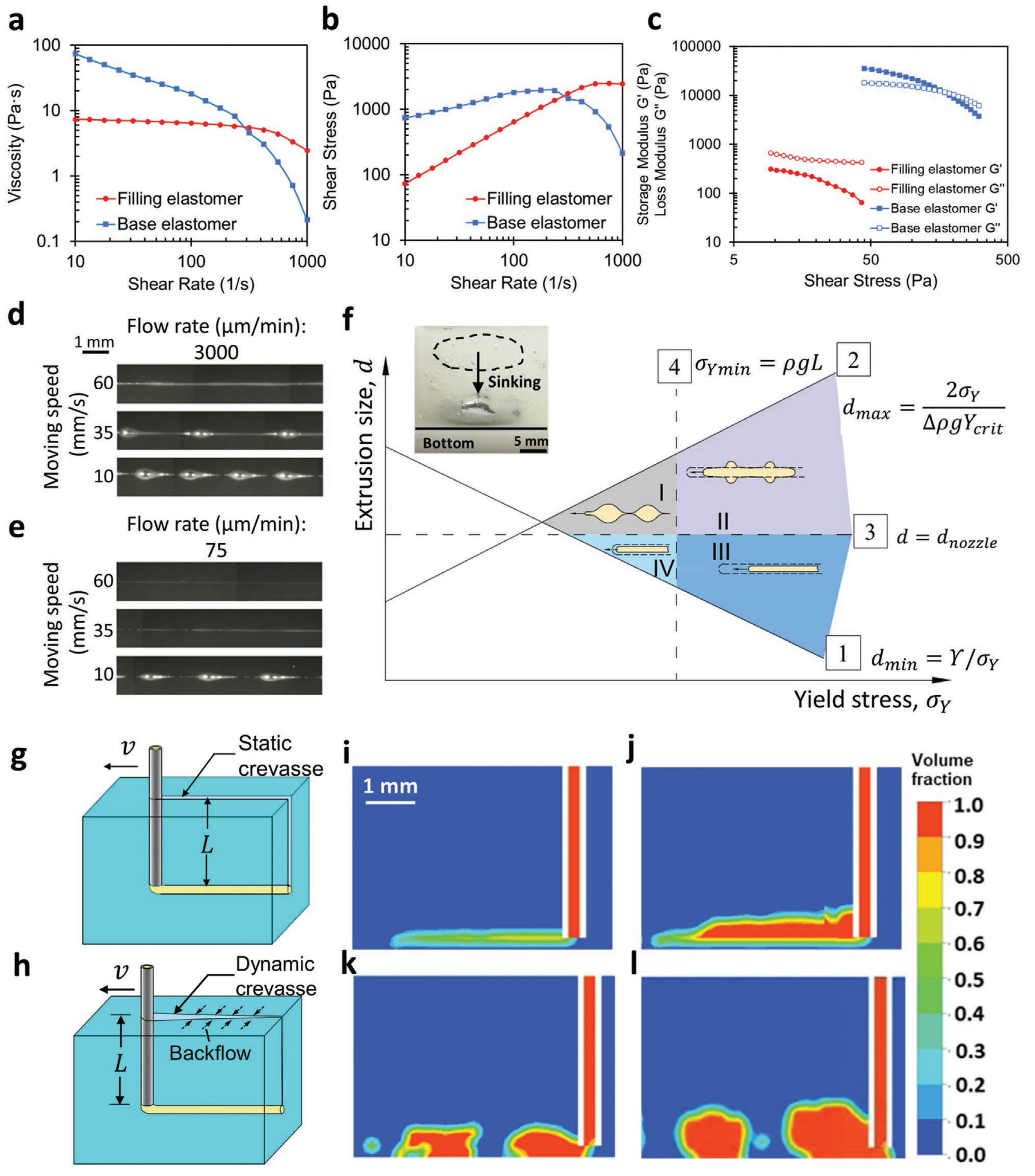

Figure 3. a) The viscosity and b) shear stress of filling and base elastomers as a function of shear rate. c) Storage modulus and loss modulus of the base and filling elastomers as functions of shear stress. d) EGaIn lines printed at a flow rate of 3000 µL min^{-1} and different moving speeds (10, 35, and 60 mm s^{-1}). e) EGaIn filaments printed at a flow rate of 75 µL min^{-1} and different moving speeds (10, 35, and 60 mm s^{-1}). f) The operation regime of embedded printing of EGaIn, where lines 1–4 are the constraints for EGaIn extruding size, the printing speed, and the elastomer yield stress and subregions I-IV are the corresponding printing settings that can be used for embedded printing. The geometries of the extruded EGaIn under different settings are listed in different subregions accordingly. When $d > d_{max}$, sinking of EGain can be observed as shown in the inset figure. g) Formation of a static crevasse in the base elastomer of high yield stress. h) Formation of a dynamic crevasse in the backflowing base elastomer of low yield stress at high printing speed. Simulation result of EGaIn under a moving speed of 60 mm s^{-1} and i) flow rate of 1500 µL min^{-1} or j) flow rate of 3000 µL min^{-1}. Simulation result of EGaIn under a moving speed of 10 mm s^{-1} and k) flow rate of 1500 µL min^{-1} or l) flow rate of 3000 µL min^{-1}.

Video S2, Supporting Information). Filament sinking occurred when the average extrusion size was too large such that the external forces applied on the filament (including gravity and buoyant force) were not in balance. Constraint line 2 defines the maximum average diameter of extrusion $d_{\max} = \frac{2\sigma_{\mathrm{Y}}}{\Delta\rho g Y_{crit}}$, below which the stress induced by the weight G of extruded EGaIn and its buoyancy F_{b} on the surrounding elastomer is less than the base elastomer's yield stress, σ_{Y}, i.e.,

$$\frac{G - F_{\mathrm{b}}}{S} < \sigma_{\mathrm{Y}} \tag{1}$$

or

$$V\Delta\rho g Y_{crit} < S\sigma_{\mathrm{Y}} \tag{2}$$

where $\Delta\rho$ is the density difference between the base elastomer and EGaIn; g is the gravitational constant; S and V are the surface area and volume of printed EGaIn droplets or filaments, respectively; and Y_{crit} is a dimensionless value of the critical yield stress below which the material acts as a solid.[31–33] This constraint allows the extruded EGaIn ink to be held at position in the base elastomer. Under this constraint, surface tension still influences the extruded shape (e.g., bulges), but it does not result in the failure of extrusion (neither breakup nor sinking).

The region between constraint lines 1 and 2 represents a typical operation regime for conventional embedded printing, which requires the use of high yield-stress, non-Newtonian fluid as the feedstock ink to facilitate material extrusion and shape retention.[16,20,21,30,34,35] For materials with high surface tension and no yield stress, such as liquid metals, this conventional operation regime does not always attain the desired printing fidelity. To identify appropriate processing conditions for liquid metals, constraint lines 3 and 4 are introduced to further divide the operation regime into subregions I-IV, as shown in Figure 3f.

Constraint line 3 specifies a critical extrusion size equal to the nozzle diameter, i.e., $d = d_{\mathrm{nozzle}}$. The subregion below line 3 ensures that the extrusion size d is less than the width of the crevasse d_{nozzle}, i.e., $d \le d_{\mathrm{nozzle}}$, thus mitigating extrusion bulges along the printing direction. This can be achieved by controlling the flow rate U of EGaIn in the nozzle to be less than the volume of the crevasse generated in unit time, i.e., $U \le \pi d_{\mathrm{nozzle}}^2 v/4$. A mechanical analogue of the EGaIn-elastomer printing model is depicted in Figure S2b in the Supporting Information (Section S2, Supporting Information) to explain the bulge formation during the printing process. Constraint line 4 (i.e., $\sigma_{\mathrm{Y}} = \rho g L$) divides the operation regime into a static crevasse sub-region (right, i.e., $\sigma_{\mathrm{Y}} > \rho g L$) and a dynamic crevasse subregion (left, i.e., $\sigma_{\mathrm{Y}} < \rho g L$) based on the relationship between the yield stress of the base elastomer and the hydrostatic pressure at the inserted depth L of the nozzle. The static crevasse subregion represents an operation regime where a static crevasse can be formed behind the nozzle (Figure 3g) and the extruded material can fill in the volume of the static crevasse, while the dynamic crevasse subregion leads to a dynamic crevasse that disappears quickly because of the backflow of the surrounding base elastomer (Figure 3h).

Among the four subregions, subregion I (gray) achieves a printing geometry with bulges connected by thin filaments, due to the small yield stress of the base elastomer and the resulting dynamic crevasse. In subregion II (purple), a static crevasse is formed, and a large extrusion size is achieved, resulting in a printing geometry with bulges connected by thicker filaments. In subregion III (dark blue), a static crevasse is formed, and an appropriate amount of EGaIn is extruded into the crevasse, enabling a uniform and continuous extrusion filament. In subregion IV (light blue) where a dynamic crevasse is formed behind the nozzle, in order to print uniform and continuous EGaIn, the nozzle has to move at a high speed in the base elastomer such that the viscous stress from the nozzle's movement on the base elastomer is greater than the gravity of the base elastomer, as described by the following inequation

$$\frac{v\eta}{d_{nozzle}} > \rho g L \tag{3}$$

where ρ and η are the density and viscosity of the base elastomer respectively and L is the crevasse's opening depth. Subregions III and IV are the operation regimes suitable for the embedded printing of EGaIn. Subregion III is the most ideal regime, where a high printing speed v and high yield stress of the elastomer σ_{Ymin} are needed to induce a static crevasse behind the nozzle. With an accurately controlled extrusion size of EGaIn and extrusion flow rate U, continuous and uniform EGaIn filaments can be printed. Nevertheless, one drawback for subregion III is that the required yield stress of the base elastomer is relatively high, which may introduce viscosity-related defects during printing, such as air bubble. Therefore, subregion IV provides an alternative for printing when the moving speed of the nozzle is well controlled to meet the requirement in Equation (3). The printing result in Figure 3d, where the moving speed was 60 mm s^{-1} and the flow rate was 3000 µm min^{-1}, was achieved in the operation regime of subregion IV.

2.4.2. Numerical Simulation

To further understand the printing fidelity of EGaIn under different process parameters, the embedded printing process was modeled in ANSYS Fluent as a two-phase flow comprising an EGaIn phase and an elastomer phase. The printing flow of EGaIn was governed by the Navier–Stokes equations (refer to

Table 1. Properties of EGaIn and base elastomer used in the numerical simulation[10,36–38].

Density of EGaIn [kg m^{-3}]	Viscosity of EGaIn [kg m s^{-}]	Density of base elastomer [kg m^{-3}]	Viscosity of base elastomer [kg m s^{-}]	Surface tension coefficient of EGaIn [N m^{-}]	Contact angle between EGaIn and walls [deg]
6250	0.00199	1062	18	0.445	140

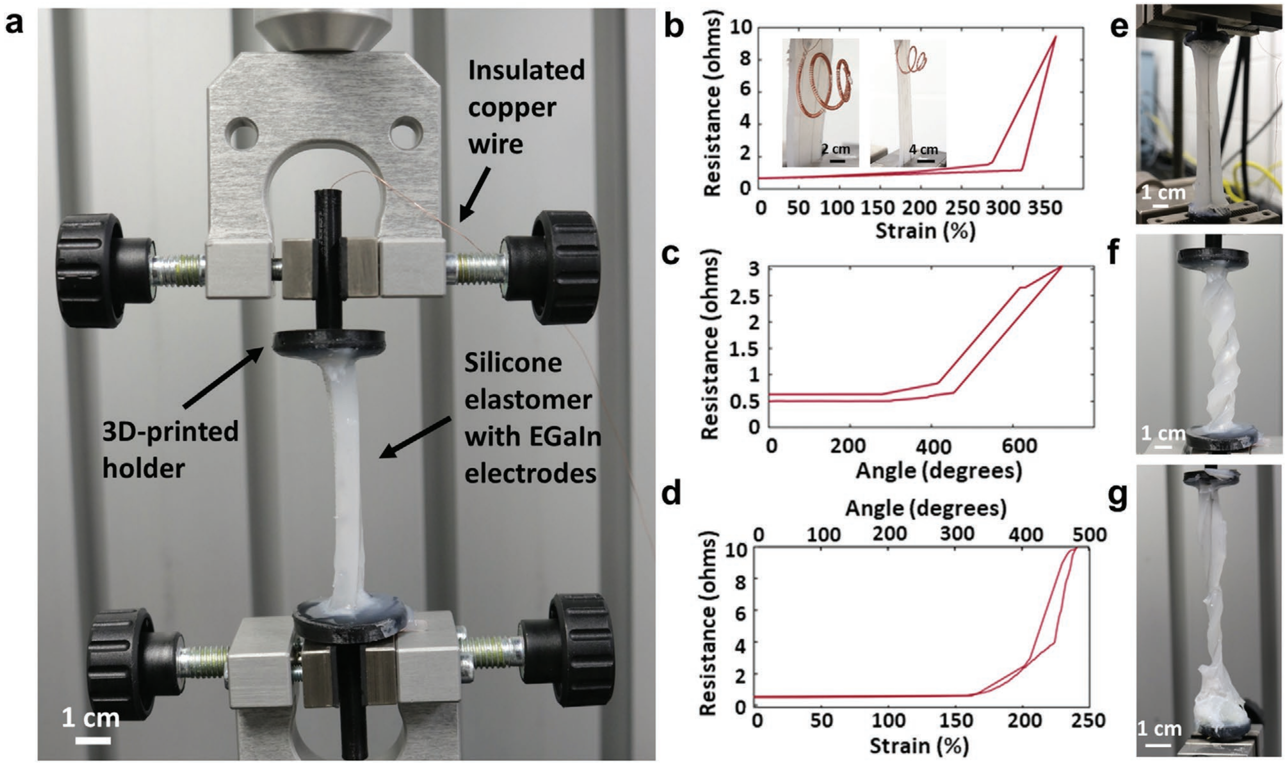

Figure 4. a) Experimental setup used for the mechanical testing of EGaIn electrodes. A single electrode was embedded inside an elastomer, and opposite ends of the elastomer were attached to a 3D-printed PLA holder. The two holders were fixed to the grippers of a tensile testing machine, and resistance of the electrode was measured in situ via copper wires using the two-point method of resistance measurement. Measured resistance variation during a b) tensile test, c) torsion test, and d) tensile-torsion test. Inset images show TSAMs actuated via the printed EGaIn electrodes with a 0% strain (left) and a 250% strain (right). e) EGaIn electrode at a maximum strain of 360%. f) Twist of 720° induced in the EGaIn electrode. g) EGaIn electrode stretched to a 230% strain and twisted to 480°.

Section S3 in the Supporting Information for more details), and the material properties used in the simulation are listed in **Table 1**. The EGaIn material was initially loaded within a nozzle, where the volume fraction α of EGaIn was equal to 1 (red). The internal and external diameters of the nozzle tube were set to the same sizes used in our experiments. The nozzle tube was then immersed in a container filled with the base elastomer material. The filling elastomer was not considered in the numerical simulation because it only acts as a healing agent for sealing the crevasse and does not influence the printing geometries. During the printing, the nozzle moved rightward with a constant moving speed v, while the EGaIn material was extruded out of the nozzle at a constant flow rate U. According to our simulation analysis, both the flow rate of EGaIn and the moving speed of the nozzle have significant impacts on the printing morphology of EGaIn. When the nozzle's moving speed was 60 mm s^{-1}, the liquid metal was printed in a continuous, uniform filament in the base elastomer with a flow rate of 1500 μL min^{-1}, as shown in Figure 3i. When the flow rate of EGaIn was increased to 3000 μL min^{-1}, a greater diameter was achieved, as shown in Figure 3j. The shapes of the simulated EGaIn filaments under different flow rates show a similar trend as the experimental results in Figure 3d,e when the flow rate was increased from 75 to 3000 μL min^{-1} under a nozzle moving speed of 60 mm s^{-1}. When the nozzle moving speed was reduced to 10 mm s^{-1}, the actual flow rate of EGaIn followed a periodic function (refer to Section 2 in the Supporting Information), leading to bulges along the printing direction as shown in Figure 3k,l.

2.5. Mechanical Testing of Embedded-Printed EGaIn Electrodes

Mechanical testing was performed to verify the electrical and mechanical stability of printed liquid metal electrodes embedded in an elastomeric matrix. **Figure 4**a depicts the experimental setup used for the mechanical testing of an elastomer (4 × 2 × 0.5 cm^3) with a printed EGaIn electrode with an internal diameter of 200 μm and a length of 5 cm. The sample was attached to 3D-printed holders that were fixed in the grippers of a tensile testing machine. Insulated copper wires were inserted into the two ends of the electrode to measure the in situ resistance of the sample using the two-point resistance method. Figure 4b–d shows the change in the resistance of the EGaIn electrode during tensile (Figure 4e), torsion (Figure 4f), and tensile-torsion tests (Figure 4g), respectively. It can be observed from Figure 4b that a 320% increase in strain led to only a 32% increase in resistance. This initial increase in resistance is due to the increase in length and simultaneous decrease in cross-sectional area of the EGaIn filament. Further stretching of the electrode caused a steep rise in the resistance, which was due to the deterioration of the contact between the

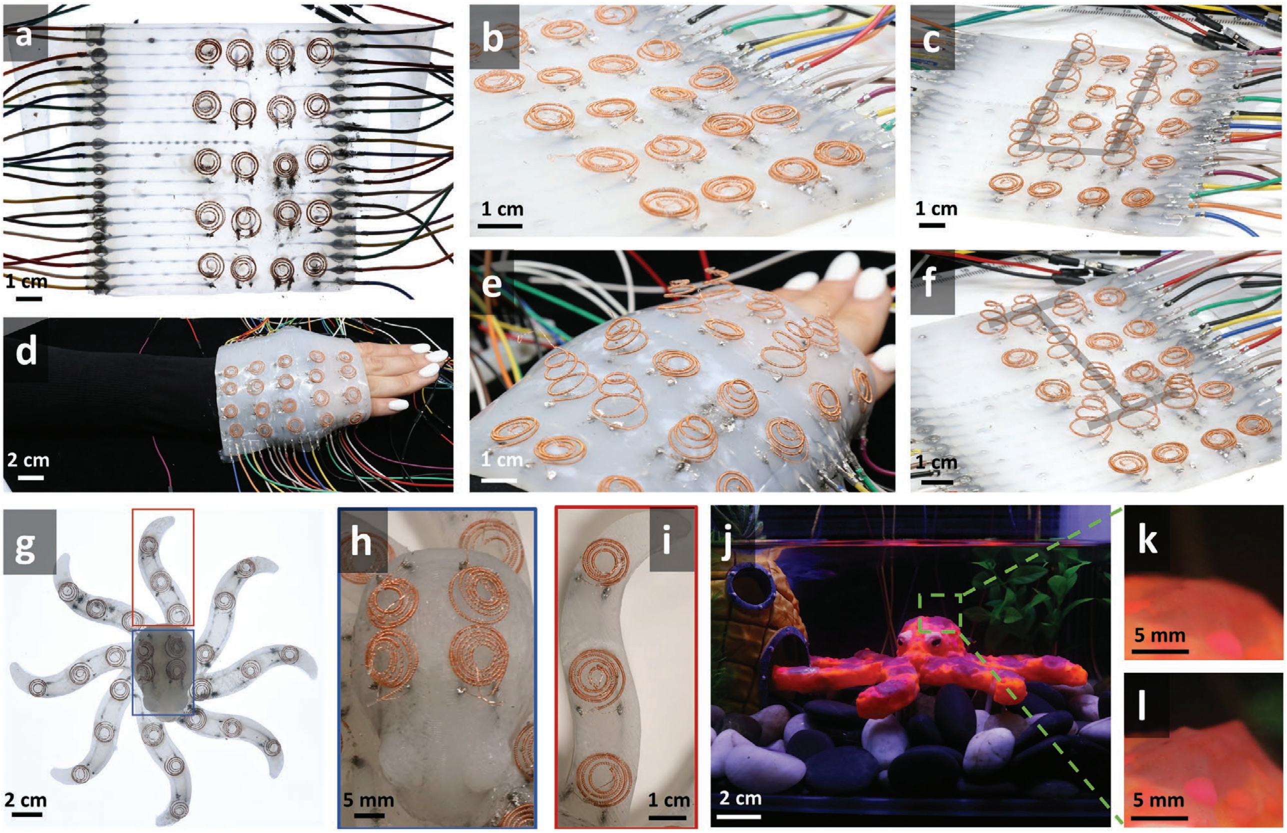

Figure 5. Test cases to illustrate the proposed shape-morphing skins based on embedded-printed EGaIn electrodes and TSAMs: a) a soft elastomeric glove containing a matrix of embedded EGaIn electrodes; b) 4 × 5 grid of TSAMs arranged on the surface of the glove; c) TSAMs actuated in U-configuration; d) glove wrapped on a hand; e) TSAM actuation on the flexible glove wrapped around a hand; f) TSAMs actuated in I-configuration; g) silicone elastomer-based octopus model with embedded elastomers and TSAMs attached to the body for texture modulation; h) close-up of TSAMs placed on a leg of the octopus; i) zoom-in of the four TSAMs on the head of the octopus; j) silicone-wrapped waterproof octopus placed in an aquarium; two TSAMs on the head of the octopus k) before and l) after actuation.

EGaIn and the pin used for measuring the resistance. A similar behavior was also observed when connecting a TSAM to an EGaIn electrode via rigid pins. It is important to note that, for efficient actuation of TSAMs, the maximum resistance of the EGaIn electrode should be less than 10 Ω. If the resistance of the electrode is too high, the current and power required to actuate the TSAMs increase substantially, which negatively influence the efficiency of the TSAM. Hence, the tensile test was terminated at a maximum strain of 360% as depicted in Figure 4b. The left inset in Figure 4b shows a TSAM activated via unstretched EGaIn electrodes, and the right inset shows a TSAM actuated via stretched EGaIn electrodes with a strain of 250%. Figure 4c represents a torsion test conducted on the EGaIn electrode. It can be seen that a twist of 420° was accompanied by a resistance increase of only 50%. A maximum twist of 720° was induced in the sample before terminating the test. Figure 4d shows the results for a tensile-torsion test wherein the sample was stretched and twisted simultaneously. A maximum strain of 230% and a maximum twist of 480° were attained before terminating the test. Additionally, it can be seen from Figure 4b–d that, by reversing the twist and stretch induced in the electrode, the resistance of the electrode dropped to its original pretest value with minimal hysteresis. These mechanical tests validate the robustness, durability, and low resistance of embedded-printed EGaIn electrodes, which can be used as flexible circuits in self-morphing smart skins for actuating TSAMs. Compared to other self-morphing structures,[2–8] the results indicate that the proposed self-morphing skins exhibited large tensile and torsional deformation (e.g., 320% tensile strain and 420° twist) with a low variation in resistance.

2.6. Test Cases for Self-Morphing Skin

A flexible elastomeric glove with a 4 × 5 grid of TSAMs was built to demonstrate the texture-modulation capability of the proposed self-morphing skin, as shown in **Figure 5**a–f; and Figure S3a (Supporting Information). TSAMs with a fiber diameter of 0.4 mm were fabricated. A total of 40 EGaIn electrodes were embedded in an elastomer matrix via embedded printing, each pair of which was used to connect one TSAM to a DC power supply, as shown in Figure 5a. The connection between each TSAM and its corresponding liquid–metal electrode pair was achieved through a rigid metal pin. One end of the pin was soldered to the terminal of the TSAM, and the other end was inserted into the liquid metal and sealed by the same elastomer. The outer spiral of each TSAM was mounted onto the elastomer surface as shown in Figure 5b. The actuation of individual TSAMs was controlled via a microcontroller (Arduino) and transistors. Figure 5c,f depicts the actuation of the glove in the configurations of "U" and "I," respectively. Figure 5d shows the flexible glove wrapped around a person's hand, while the texture-modulation behavior of the wearable device is depicted in Figure 5e. Actuation of the glove can also be seen in Video S3 (Supporting Information).

A silicone elastomer replica of an octopus with TSAMs on its surface was also fabricated to mimic the texture-modulation behavior of octopi. Figure 5g depicts the arrangement of TSAMs on the octopus. Three TSAMs were attached to each leg, and four TSAMs were mounted on the head of the octopus as shown in Figure 5h,i, respectively. Figure 5g and Figure S3b (Supporting Information) also illustrate the EGaIn electrical circuit embedded inside a silicone matrix for establishing connections between the TSAMs and a power supply. Four curved electrodes were printed in the head, and two electrodes were embedded in each leg. Rigid metal pins were used to connect the TSAMs to the liquid metal electrodes. Additionally, the octopus model was covered with a thin layer of elastomer and airbrushed with silicone-based color pigments to highlight the octopus body and TSAMs as shown in Figure 5j. The completely waterproof octopus was then placed in an aquarium and tested underwater. Figure 5k,l depicts two TSAMs on the head of the octopus before and after actuation, respectively. This test case highlights the feasibility of electrothermal actuation of the proposed waterproof self-morphing skin comprising liquid metal electrodes and TSAMs in an underwater environment that imitates the texture-modulation behavior of cephalopods.

3. Conclusion

A cephalopod-inspired stretchable, self-morphing skin is proposed in this paper. Texture modulation is achieved via TSAMs that can perform vertical displacement with a strain of 2000% under electrothermal actuation within few seconds. An embedded printing method was employed to print flexible, low-resistance, and robust low-viscosity Newtonian liquid metal electrodes within a flexible elastomer. The printing was enabled by tailoring the printing parameters toward the subregions of static crevasse formation in the operation regime of traditional embedded printing processes. Theoretical and numerical models were developed to explain the effects of different printing parameters on the geometrical fidelity of the embedded-printed EGaIn electrodes. With the guidance of the model, optimum printing strategies were identified to fabricate continuous, uniform EGaIn electrodes with low resistance that can connect and actuate TSAMs with programable patterns. Mechanical tests were performed to exhibit the electrical and mechanical stability of the self-morphing skin. The skin sustained a tensile deformation of 320% and a torsional twist of 420° with a low variation in resistance. A wearable glove and a shape-changing replica of an octopus were fabricated and tested with different programmable patterns and working environments. The test cases validate the suitability of the proposed self-morphing skins to function as a wearable and waterproof self-morphing device. These results offer the potential to fabricate more complex stretchable, self-morphing skins that will be viable for applications ranging from refreshable Braille displays and haptic feedback devices to underwater turbulence tripping and antifouling devices.

4. Experimental Section

Fabrication of TSAMs: TSAMs were manufactured from inexpensive, commercially available nylon fishing lines.[25] The fabrication process of TSAMs involved the following six steps: 1) a polymer fishing line of the required diameter was twisted using a hand drill; 2) an insulated copper wire was folded in half and attached to the chuck of the drill; 3) an additional twist was inserted into the fishing line, and at the same time the copper wire was helically wrapped around the fishing line. Twisting was applied until the polymer line started coiling simultaneously; 4) the twisted portion of the fishing line was then manually formed into a flat Archimedean spiral on an adhesive substrate; 5) the muscle was then annealed at 150 °C for 3 h to retain the spiral shape; and 6) after cooling, the TSAMs were allowed to reach an equilibrium state for 48 h before electrothermal actuation.[9] Alternatively, silver paint, instead of copper wire, can be used to provide electrical conductivity to TSAMs.[39]

Copper wire was used for the electrothermal actuation of TSAMs because of its excellent electrical conductivity, low cost, and ability to provide joule heating during electrothermal actuation of the TSAMs. Furthermore, copper wire contributes to the mechanical stiffness of a TSAM that improves the actuation performance of the artificial muscle.[9] In the previous work,[39] the authors coated polymer fishing lines with silver paste for the electrothermal actuation of TSAMs. However, it proved to be challenging to obtain a reliable, uniform coating. It would be similarly difficult to coat fishing lines with liquid EGaIn due to its low viscosity. Meanwhile, unlike silver paste, EGaIn does not flash dry in air, and the coating would thus peel off instantaneously. Therefore, as compared to silver- or liquid–metal-coated samples, the actuation behavior of copper-wrapped TSAMs was more repeatable and reliable.

Base Elastomer: Uncured part A and part B of silicone elastomers, FX-Pro (Smooth-On, East Texas, PA), were first mixed using a weight ratio of 1:1. A cure retarder, Slo-Jo (Smooth-On, East Texas, PA), was added into the FX-Pro mixture at a concentration of 2 wt% to slow down the curing rate of the base elastomer in air. A thickening solution, Thi-vex (Smooth-On, East Texas, PA), was then added at a concentration of 2 wt% to increase the viscosity of the elastomer.

Filling Elastomer: Similar to the base elastomer, part A and part B of FX-Pro were first mixed using a weight ratio of 1:1. Slo-Jo and a thinner solution, Silicone Thinner (Smooth-On, East Texas, PA), were added to the FX-Pro mixture at concentrations of 5 and 10 wt%, respectively. Silicone Thinner was added to lower the viscosity of FX-Pro for better flowability. Additional Slo-Jo was added to the filling elastomer to slow down the curing rate since it rested atop the base elastomer and had a larger area exposed to the air. Both the base and filling elastomers were mixed for 2 min and degassed using a vacuum for 8 min.

Eutectic Gallium–Indium (EGaIn): EGaIn (Ga 75.5%, In 24.5%) material was purchased from Sigma-Aldrich and used as received.

Embedded Printing: A three-axis robot (Janome-Roboter JR-2303N, Nordson, Westlake, OH) was used to control the extrusion nozzle. A syringe dispenser was mounted on the robot arm, which was driven by a linear actuator (NE-1000 Programmable Single Syringe Pump, New Era Pump Systems, Farmingdale, NY). The syringe needle has an inner diameter of 0.25 mm and an external diameter of 0.52 mm. The electrodes embedded in the stretchable morphing glove and cephalopod were printed using a constant moving speed of 60 mm s^{-1} for the needle and a flow rate of 3000 μL min^{-1} for the EGaIn extrusion.

Rheological Tests: The rheological properties of the base and filling elastomers were measured using a modular compact rheometer (MCR 72, Anton Paar, Ashland, VA) equipped with 25 mm diameter parallel plates (PP25, 1 mm gap). The viscosity and shear stress tests were measured for both elastomers under shear rates ranging from 10 to 1000 s^{-1}. The amplitude sweep tests were performed at a fixed angular frequency of $\omega = 100$ rad s^{-1}. The yield stress for both elastomers was calculated as the intersection point of the elastic modulus and loss modulus curves. All the tests were conducted at room temperature (25 °C).

Mechanical Tests: A tensile testing machine (131ATV Series Frame, Test Resources, Shakopee, MN) was used for the mechanical testing of the flexible electrodes. A digital multimeter (Keysight Technologies, Santa Rosa, CA, Model 34470A) was used for two-point in situ resistance measurements. Real-time resistance was recorded using the PathWave BenchVue Software (Keysight Technologies, Santa Rosa, CA, Model 34470A). The EGaIn embedded electrode was attached to two polylactic acid (PLA) holders, which were 3D printed using a fused deposition modeling (FDM) printer (Raise 3D Technologies, Irvine, CA). 36 AWG insulated copper wire (Remington Industries, Johnsburg, IL) was used to connect the electrode to the multimeter. For each mechanical test, the electrode sample was attached to the 3D-printed holders via a silicone elastomer (Dragon Skin FX-Pro, Smooth-On, Macungie, PA). The tensile test was performed by fixing the sample containing the holders in the grippers of the tensile testing and then moving the upper end at a rate of 0.5 mm s^{-1}. On the other hand, the torsion test was carried out by fixing the upper end of the sample and slowly rotating the lower end counterclockwise at a rate of 6° s^{-1}. Finally, the tensile-torsion test involved simultaneous stretching (0.5 mm s^{-1}) and twisting (6° s°) of the sample.

Test Cases of Self-Morphing Skin: The models of the glove and octopus were fabricated by printing EGaIn electrodes in 3D-printed PLA molds filled with base and filling elastomers. The design of the models is provided in the Supporting Information. 20 TSAMs were fixed on the glove, and 28 TSAMs were attached to the body of the octopus (3 on each leg and 4 on the head). Rigid metal pins were soldered to the terminals of each TSAM. These pins easily pierced through the elastomer and maintained a constant electrical connection between the TSAM and EGaIn electrodes. The outer tip of each TSAM was affixed to the surface of the test model to ensure that the TSAM did not translate horizontally during actuation. A DC power supply (Longwei Instruments, Tangxia, Dongguan, Guangdong, China) was used for the electrothermal actuation of the TSAMs, and the supplied power was controlled using an Arduino Uno and a transistor (TIP122, ON Semiconductor, Phoenix, AZ) for individual actuation of each muscle. The octopus was completely covered with an extremely thin layer of silicone elastomer (EcoFlex 00-30, Smooth-On, Macungie, PA) that was manufactured using a spin coater (Spincoat G3P-8, Specialty Coating Systems, Indianapolis, IN). The outer elastomer coating was attached to the octopus using small amounts of uncured elastomer. Additionally, the octopus was airbrushed using a flexible platinum silicone-based paint (Psycho Paint, Smooth-On, Macungie, PA) containing silicone orange and purple pigments (Silc Pig Electric, Smooth-On, Macungie, PA).

Supporting Information

Supporting Information is available from the Wiley Online Library or from the author.

Acknowledgements

F.F., P.K., and L.H. contributed equally to this work. C.L. acknowledges support from the Office of Naval Research, Grant Nos. N00014-19-1-2136 and N00014-20-1-2224. X.S. acknowledges support from National Science Foundation under Grant No. 1825962.

Conflict of Interest

The authors declare no conflict of interest.

Data Availability Statement

Research data are not shared.

Keywords

cephalopods, embedded printing, smart skin, texture modulation, twisted spiral artificial muscles

Received: June 9, 2021
Revised: August 9, 2021

---

[1] J. J. Allen, G. R. Bell, A. M. Kuzirian, R. T. Hanlon, *J. Morphol.* **2013**, *274*, 645.
[2] H. Thérien-Aubin, Z. L. Wu, Z. Nie, E. Kumacheva, *J. Am. Chem. Soc.* **2013**, *135*, 4834.
[3] J. Kim, J. A. Hanna, M. Byun, C. D. Santangelo, R. C. Hayward, *Science* **2012**, *335*, 1201.
[4] E. Wang, M. S. Desai, S.-W. Lee, *Nano Lett.* **2013**, *13*, 2826.
[5] Q. Ge, A. H. Sakhaei, H. Lee, C. K. Dunn, N. X. Fang, M. L. Dunn, *Sci. Rep.* **2016**, *6*, 31110.
[6] T. H. Ware, M. E. McConney, J. J. Wie, V. P. Tondiglia, T. J. White, *Science* **2015**, *347*, 982.
[7] J. Pikul, S. Li, H. Bai, R. Hanlon, I. Cohen, R. Shepherd, *Science* **2017**, *358*, 210.
[8] Y. Hu, Z. Zhao, A. Vimal, G. Hoffman, presented at *2018 IEEE International Conference on Soft Robotics (RoboSoft)*, IEEE, Piscataway, NJ **2018**.
[9] C. Lamuta, H. He, K. Zhang, M. Rogalski, N. Sottos, S. Tawfick, *Adv. Mater. Technol.* **2019**, *4*, 1900260.
[10] M. D. Dickey, R. C. Chiechi, R. J. Larsen, E. A. Weiss, D. A. Weitz, G. M. Whitesides, *Adv. Funct. Mater.* **2008**, *18*, 1097.
[11] E. S. Elton, T. C. Reeve, L. E. Thornley, I. D. Joshipura, P. H. Paul, A. J. Pascall, J. R. Jeffries, *J. Rheol.* **2020**, *64*, 119.
[12] D. M. Vogt, Y.-L. Park, R. J. Wood, *IEEE Sens. J.* **2013**, *13*, 4056.
[13] R. K. Kramer, C. Majidi, R. J. Wood, *Adv. Funct. Mater.* **2013**, *23*, 5292.
[14] T. Jung, S. Yang, *Sensors* **2015**, *15*, 11823.
[15] A. C. Siegel, D. A. Bruzewicz, D. B. Weibel, G. M. Whitesides, *Adv. Mater.* **2007**, *19*, 727.
[16] H. Ota, S. Emaminejad, Y. Gao, A. Zhao, E. Wu, S. Challa, K. Chen, H. M. Fahad, A. K. Jha, D. Kiriya, *Adv. Mater. Technol.* **2016**, *1*, 1600013.
[17] A. Tabatabai, A. Fassler, C. Usiak, C. Majidi, *Langmuir* **2013**, *29*, 6194.
[18] Y. Zheng, Z.-Z. He, J. Yang, J. Liu, *Sci. Rep.* **2014**, *4*, 4588.
[19] Q. Wang, Y. Yu, J. Yang, J. Liu, *Adv. Mater.* **2015**, *27*, 7109.
[20] J. T. Muth, D. M. Vogt, R. L. Truby, Y. Mengüç, D. B. Kolesky, R. J. Wood, J. A. Lewis, *Adv. Mater.* **2014**, *26*, 6307.
[21] A. K. Grosskopf, R. L. Truby, H. Kim, A. Perazzo, J. A. Lewis, H. A. Stone, *ACS Appl. Mater. Interfaces* **2018**, *10*, 23353.
[22] M. Wehner, R. L. Truby, D. J. Fitzgerald, B. Mosadegh, G. M. Whitesides, J. A. Lewis, R. J. Wood, *Nature* **2016**, *536*, 451.
[23] L. y. Zhou, J. z. Fu, Q. Gao, P. Zhao, Y. He, *Adv. Funct. Mater.* **2020**, *30*, 1906683.
[24] J. Finn, M. Norman, Octopus maorum, https://collections.museumsvictoria.com.au/species/8694 (accessed: June 2021).
[25] C. S. Haines, N. Li, G. M. Spinks, A. E. Aliev, J. Di, R. H. Baughman, *Proc. Natl. Acad. Sci. USA* **2016**, *113*, 11709.
[26] L. Parth Kotak, T. Weerakkody, Caterina, *Polymer* **2021**, *222*, 123642.

[27] L. He, F. Fei, W. Wang, X. Song, *ACS Appl. Mater. Interfaces* **2019**, *11*, 18849.

[28] D. Fraggedakis, Y. Dimakopoulos, J. Tsamopoulos, *Soft Matter* **2016**, *12*, 5378.

[29] M. Garín, C. Jin, D. Cardador, T. Trifonov, R. Alcubilla, *Sci. Rep.* **2017**, *7*, 7233.

[30] C. S. O'Bryan, T. Bhattacharjee, S. R. Niemi, S. Balachandar, N. Baldwin, S. T. Ellison, C. R. Taylor, W. G. Sawyer, T. E. Angelini, *MRS Bull.* **2017**, *42*, 571.

[31] M. Beaulne, E. Mitsoulis, *J. Non-Newtonian Fluid Mech.* **1997**, *72*, 55.

[32] A. Beris, J. Tsamopoulos, R. Armstrong, R. Brown, *J. Fluid Mech.* **1985**, *158*, 219.

[33] H. Emady, M. Caggioni, P. Spicer, *J. Rheol.* **2013**, *57*, 1761.

[34] W. Wu, A. DeConinck, J. A. Lewis, *Adv. Mater.* **2011**, *23*, H178.

[35] C. S. O'Bryan, T. Bhattacharjee, S. Hart, C. P. Kabb, K. D. Schulze, I. Chilakala, B. S. Sumerlin, W. G. Sawyer, T. E. Angelini, *Sci. Adv.* **2017**, *3*, e1602800.

[36] I. Smooth-On, *Dragon Skin FX-Pro* https://www.smooth-on.com/products/dragon-skin-fx-pro/ (accessed: January 2021).

[37] Sigma-Aldrich, Gallium–Indium eutectic, https://www.sigmaaldrich.com/catalog/product/aldrich/495425?lang=en&region=US&gclid=CjwKCAiAgJWABhArEiwAmNVTB9XYsfZyPUgVAuM7gkkfxEx5H-hkwB1J_eYzt0nteyqpISZlWP-YUbxoCUyMQAvD_BwE (accessed: January 2021).

[38] Q. Xu, N. Oudalov, Q. Guo, H. M. Jaeger, E. Brown, *Phys. Fluids* **2012**, *24*, 063101.

[39] C. Greco, P. Kotak, J. K. Gallegos, J. Fang, A. Wilkinson, L. Pagnotta, C. Lamuta, *Manuf. Lett.* **2020**, *26*, 11.